Chapter 5

Effect of Sr-doping on the electrochemical Pseudocapacitance of $Y_{1-x}Sr_xMnO_{3-\delta}$ perovskites

In this study, Sr-doped $YMnO_3$ i.e. $Y_{1-x}Sr_xMnO_{3-\delta}$ perovskite was prepared by the solid-state ceramic route and studied for electrochemical pseudocapacitance in aqueous 2M KOH electrolyte. The formation of the mostly cubic phase, with 50% strontium doped $YMnO_3$ (YSMO-50) provides an equivalent three-dimensional network and superior conductivity due to Mn^{3+}–O^{2-}–Mn^{4+} hopping conduction. Further, Redox-mediated interconversion of oxide to hydroxide ($M^{2+}O^{2-} + H_2O + e^- \leftrightarrow M^+OH^- + OH^-$) in aqueous media is shown to be the reason behind the high capacitance of YSMO-50. The excellent electrochemical performance of YSMOs was attributed to the reversible interconversion of oxide-ion into hydroxide ion coupled with surface redox reaction of Mn^{2+}/Mn^{3+} and Mn^{3+}/Mn^{4+} occurring at the electrode surface. The maximum energy density of 65.13 W h kg^{-1} was achieved at a power density of 0.45 kW kg^{-1} for an asymmetric mode, in which YSMO serves as a negative electrode and Activated carbon (AC) as a positive electrode in the PVA–KOH gel electrolyte. Our study reveals that the doping of low valence atom (Sr) at the A-site in perovskite manganite ($YMnO_3$) may be an effective tool to enhance the pseudocapacitive performance of perovskite-based electrodes.

5.1 Introduction

The reversible intercalation and diffusion of anions into the perfectly ordered structure are quite difficult due to their relatively large size. Recently, perovskite-structure (ABO_3)[198] and its other derivatives such as double perovskite oxides ($AA'BB'O_6$)[199] and Ruddlesden–Popper perovskites {$(AO)(ABO_3)n$ [200] has been considered as a supercapacitor electrode because of its ability to attain a large number of oxygen vacancies in its structure. In 2014, Mefford et al. reported anion-intercalation type pseudocapacitance for $LaMnO_3$ perovskite in which oxygen-vacancy mediated redox has been applied for fast charge storage [117]. Since then, several perovskite metal oxides and their derivatives, such as; $LaSrO_{3-\delta}$, $La_xSr_{1-x}CoO_{3-\delta}$, $La_xSr_{1-x}Cu_{0.1}Mn_{0.9}O_{3-\delta}$, $La_xSr_{1-x}Co_{0.1}Mn_{0.9}O_{3-\delta}$, La_2CoMnO_6, $La_{0.85}Sr_{0.15}MnO_3$, $LaFeO_3$, $LaNiO_3$, $La_{1-x}Ca_xMnO_3$, and $LaMnO_3$@CC-PPy have been extensively studied as supercapacitor electrodes.

The charge-storage mechanisms in perovskite materials are mainly due to reversible oxide anion intercalation/de-intercalation and oxygen vacant sites are the main charge-storage sites in perovskites. Therefore, the energy densities of perovskite electrodes can be enhanced by introducing oxygen vacancies. Liu et al. studied the electrochemical performance of $PrBaMn_2O_{6-\delta}$ (f-PBM) and reduced $PrBaMn_2O_{6-\delta}$ (r-PBM) and found that r-PBM with a single cubic phase exhibited metallic character in its ground state whereas f-PBM with hexagonal structure has a small band gap of 1.39 eV, exhibiting poor conductivity, as compared to cubic phase [201]. Therefore, oxygen vacancy formation energy for the cubic phase is less compared to its hexagonal phase and can affect the oxygen diffusion rate and conductivity of the electrode. Further, Elsiddig showed that the electrochemical properties of $LaMnO_3$ can be enhanced by creating oxygen vacancies in its structure. However, Tabari et al. found that the formation of large numbers of oxygen vacancies in $La_{1-x}Ca_xMnO_3$ harms electrochemical properties because of the generation of a lot of Mn^{4+} ions by calcium doping, which may decline the charge transfer ability of the electrode [202]. Because of the above facts, it has been concluded that pseudocapacitance arises not only because of oxygen vacancies but also depends on the electrical conductivity of the electrode materials.

Redox-mediated interconversion of oxide to hydroxide ($M^{2+}O^{2-} + H_2O + e^- \leftrightarrow M^+OH^- + OH^-$) in aqueous media is shown to be the reason behind high capacitance in perovskite-based

materials. Thus, the interconversion efficiency in perovskite materials is not only limited upon the formation of oxygen vacancy but also, depends on the availability of redox structure (operating redox couple) and electron transfer rate or conductivity of the materials.

In the present work, Sr-doped $YMnO_3$ samples were successfully synthesized by the solid-state ceramic route, and their electrochemical pseudocapacitance as anode materials were investigated by cyclic voltammetry, galvanostatic charge/discharge, and electrochemical impedance methods. In stoichiometric $YMnO_3$, the Mn is present usually in a 3+ oxidation state, as we dope low-valence Sr atom at Y sites, Mn^{3+} oxidized to Mn^{4+} oxidation state which may lead to the lattice distortion in $YMnO_3$ structure and enhances the electrical conductivity of the materials through Mn^{3+}-O^{2-}-Mn^{4+} hopping conduction. The doping of higher ionic radii Sr^{2+} at the place of smaller Y^{3+} may change the M–O–M angle and M–O bond length which can transform the crystal structure from hexagonal to cubic. To verify that strontium-doping could increase the specific capacitance of the electrode, the performance of the electrode, as well as the mechanism of anion-interconversion charge, was examined through changes in the valence state of manganese during the charge–discharge process. Further, we have demonstrated a full cell using 50% Sr doped $YMnO_3$ and activated carbon (AC) as anode and cathode material respectively, to assemble asymmetric cells and the fabricated device exhibited superior performance as an anion-interconversion type electrode for supercapacitor.

5.2 Experimental

5.2.1 Materials synthesis

The solid-state ceramic synthesis route was adopted to obtain crystalline Sr-doped $Y_{1-x}Sr_xMnO_3$ (x = 0, 0.2, 0.5, 0.7, 1.0) because this route produces more thermodynamically stable products. Y_2O_3 (99.9%), $SrCO_3$ (99.9%), and $MnCO_3$ (99.9%) were taken in a stoichiometric ratio and mixed in an agate mortar pestle for about 60 min. The mixture was first fired at 600 °C and then calcined at 1000 °C for 12 h in an alumina crucible for the preparation of $YMnO_3$ and $Y_{1-x}Sr_xMnO_3$ (x = 0.2, 0.5, 0.7, 1.0) followed by slow cooling to room temperature to get phase pure materials. The samples were denoted as YSMO-0, YSMO-20, YSMO-50, YSMO-70, and YSMO-100 for 0, 20, 50, 70, and 100% Sr-doped $YMnO_3$, respectively, in the whole manuscript.

5.2.2 Material characterizations

The crystallinity and phase identification of the prepared materials were confirmed by room temperature X-ray diffraction (XRD) using Cu-Kα radiation (l = 1.54 Å) operated at 40 kV and 15 mA between 2Θ of 10°–80° at a scan rate of 2° per min and 0.02° per step size in Bragg–Brentano configuration. The structures were refined by the Rietveld refinement method using FULLPROF suite software. The microstructures of the sintered samples were investigated using a scanning electron microscope (EVO-Scanning Electron Microscope MA15/18) equipped with an EDS system and the lattice fringes were obtained by taking HR-TEM (FEI TECNAI G2 20 TWIN) images operated at 300 kV. X-ray photoelectron spectroscopy (XPS) studies were carried out using a Thermo Scientific Multilab 2000 instrument with Al Kα radiation operated at 150 W to investigate the electronic structures of the materials. All the binding energy values were charge-corrected to adventitious C 1*s* at 284.5 eV and the peak deconvolution has been done with the help of XPSPEAK41 software. The oxidation state of manganese (Mn) and oxygen stoichiometry were determined by using a chemical redox titration method. 50 mg of active materials were dissolved in 25 mL of hydrochloric acid (3 M) in the presence of 24 mg of potassium iodide (KI), and the liberated iodine was titrated against the sodium thiosulfate $Na_2S_2O_3$ (1 M) using starch as an indicator. The triplet reading was taken for oxygen stoichiometry with an error of 0.01. Prior experiment, high-purity argon gas was bubbled into the solution to avoid oxygen contamination from the air.

5.2.3 Electrochemical measurements

Electrochemical measurements were performed with the help of an electrochemical workstation based on the Pine research instrument (Wave driver 200). A three-electrode setup consisting of active material coated carbon paper of area 1 cm^2 as a working electrode, Hg/HgO/20% KOH as a reference electrode, and a platinum wire as a counter electrode, respectively, was used. The working electrode was prepared by mixing synthesized active material (35 mg) conducting activated carbon (10 mg) and polyvinylidene difluoride (PVDF) (5 mg) as a binder in 2 ml of N-methyl pyrrolidone (NMP), which was used as a solvent. To investigate the activity of the supercapacitors, an aliquot of 40 μL of homogenized ink was deposited by a micropipette onto the surface of a carbon paper (1 cm^2) and dried under an IR

lamp and kept at 80 °C in an electric oven for 12 hr. The mass of the active material loaded on the substrate was approximately 1 mg. Electrochemical analysis was done with the help of Aftermath software by performing cyclic voltammetry, galvanostatic charge/discharge, and electrochemical impedance spectroscopy in a 2 M KOH aqueous electrolyte.

The CVs were measured at scan rates from 2 to 50 mV s^{-1} within the potential window of -0.8 to 0.2 V. The GCD curves were recorded at various current densities of 0.5 to 5 A g^{-1} in the same potential window as CVs. The EIS (Electrochemical Impedance Spectroscopy) measurements of all the samples were conducted in the frequency range between 100 kHz to 0.1 Hz with an alternating current (AC) amplitude of 10 mV at open-circuit voltage. The specific capacitances (C_s ($F\ g^{-1}$)) were evaluated from the CV and GCD curves according to the following Eq. (5.1) and (5.2):

$$C_s(F\ g^{-1}) = \frac{\int I(V)dV}{2m\upsilon\Delta V} \dots\dots (5.1)$$

Where $\int I(V)dV$ is the area integrated under the CV curve, m(g) is the mass of active material, υ (V s^{-1}) is the scan rate and $\Delta V(V)$ is the potential window.

$$C_s(F\ g^{-1}) = \frac{I\ t_d}{m\Delta V} \dots\dots (5.2)$$

Where $I(A)$ is the discharge current, $t_d(s)$ is discharge time, $m(g)$ is the mass of active material and $\Delta V(V)$ is the potential window.

5.3 Results and Discussions

5.3.1 XRD study

The two most important parameter that affects the anion intercalation mechanism of a supercapacitor electrode is its crystal structure and the specific surface area. The phase structure has an important influence on the formation of oxygen vacancies that decide the oxygen ion diffusion rate in the perovskite material, hence affecting its capacity, rate capability, and cyclic performance[201]. The crystallinity and phase identification of the samples with different strontium content in $Y_{1-x}Sr_xMnO_3$ perovskite were confirmed by XRD measurement in 2θ range of 10°−80° as presented in Fig. 5.1(a).

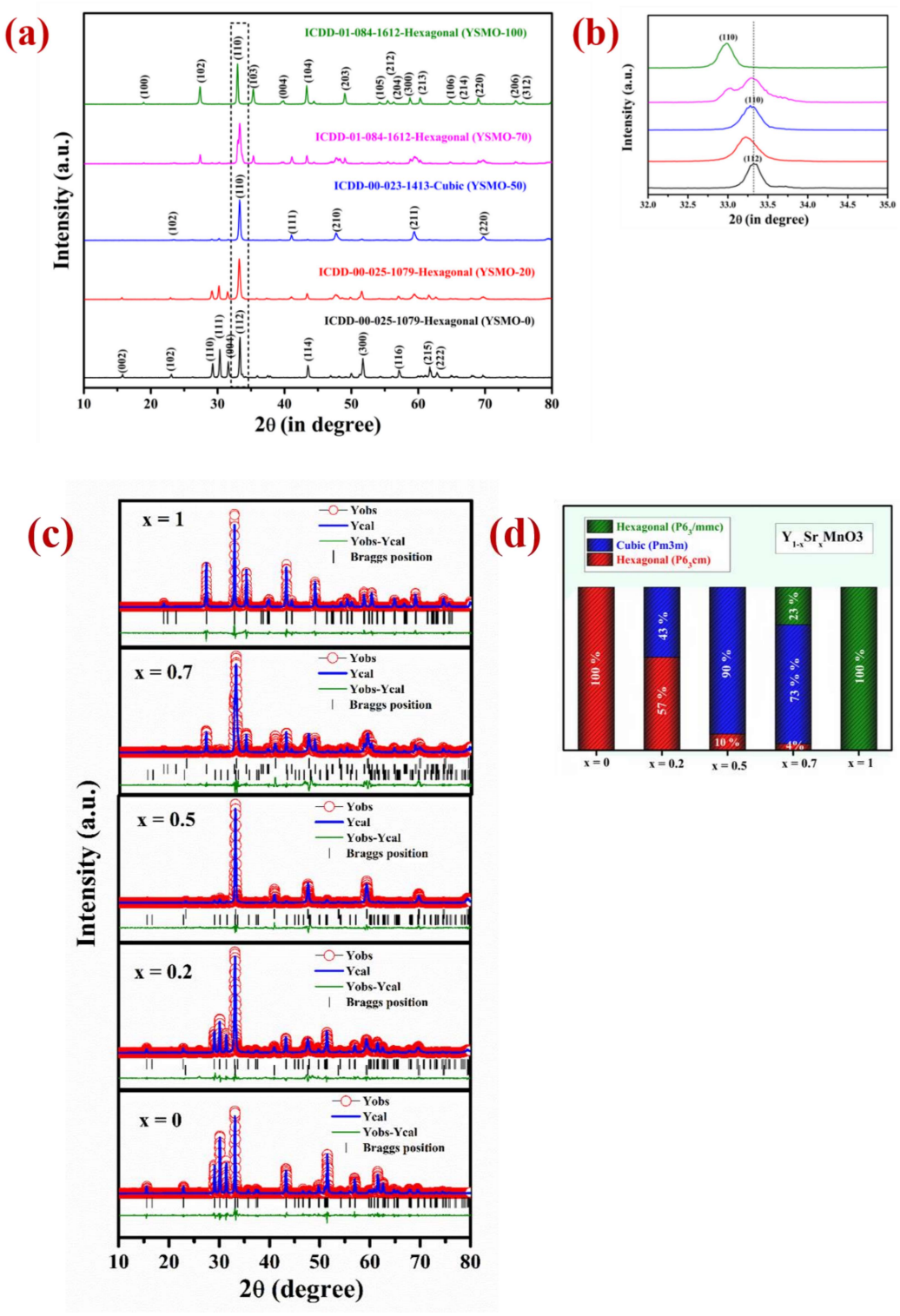

Figure 5.1: (a) the XRD pattern in 2Θ range 10-80°, (b) the zoom image in 2Θ range 32-35°. (c) Rietveld refinement study collected in 2Θ range 10-80° and (d) shows % phase fraction analysis of different YSMOs samples.

The strong diffraction peaks for YSMO-0 were observed at (110), (111), (004), and (112), which correspond to the hexagonal phase of $YMnO_3$ having space group $P6_3cm$ (ICDD-00-025-1079). As the concentration of strontium increases, the crystal structure has changed. At lower Sr concentration (x = 0.2), along with the hexagonal ($P6_3cm$) phase, a weak diffraction peaks at (110), (111), (200), (211), and (220) of cubic phase having space group (Pm3m) has appeared, that indicates mixed phase formation (hexagonal and cubic) in YSMO-20. At x = 0.5, the cubic phase becomes more pronounced at the expense of the hexagonal phase ($P6_3cm$), as the XRD pattern of YSMO-50 shows mostly diffraction peaks corresponding to the cubic phase with a negligible amount of hexagonal phase in YSMO-50. On further increasing the strontium concentration, the crystal structure again distorts and adopts a hexagonal structure with a different atomic arrangement. The XRD pattern of YSMO-70 (x = 0.7) showed weak diffraction peaks at (102), (110), (103), (202), and (203) that correspond to hexagonal phase having space group $P6_3/mmc$ (ICDD-01-084-1612) along with cubic phase. When Y is completely replaced by Sr-atom, the structure adopts pure hexagonal form as the XRD pattern of YSMO-100 shows a pure hexagonal phase having space group $P6_3/mmc$. No diffraction peaks corresponding to the Y_2O_3 phase is found in any of the Sr-doped $YMnO_3$ samples. This suggests that Sr^{2+} ions substitute Y^{3+} ions in all three phases. Further, we have performed Rietveld refined study on all samples using the FULLPROF program and pseudo-Voigt as the peak profile function, shown in Fig. 5.1(c). The experimental, calculated, and their difference patterns were denoted as a solid, dotted, and continuous bottom line, respectively. It is worth mentioning that the incorporation of Sr^{2+} ions in the $YMnO_3$ lattice distorts the lattice and at 50% doping, significantly shifted the crystal structure from hexagonal to cubic, which further turned to a different hexagonal phase upon complete substitution of Y^{3+} by Sr^{2+} ions. From the refinement data, we have estimated the phase fraction, the values of the lattice parameters (a, b, and c), unit cell volume (v), and reliability factors (χ^2) of different YSMOs samples, and listed in Table 5.1. Figure 5.2 represents the crystal structure showing different patterns of MnO_6 octahedra in various synthesized YSMOs. Since the ionic radius of Y^{3+} is smaller than Sr^{2+}, the average ionic radii on the A site increases after doping, hence, the most intense diffraction peak (110) observed at 33^o was shifted towards lower 2θ values, as shown in Fig. 5.1(b).

Table 5.1: Structural analysis of different composition of $Y_{1-x}Sr_xMnO_3$

Composition	Phases	Phase fraction	Unit cell parameters	Unit cell volume	χ^2
YSMO-0 **($YMnO_3$)**	Hexagonal ($P6_3cm$)	100 %	a = b = 6.143(11) c = 11.395(4)	v = 372.457	1.84
YSMO-20 **($Y_{0.8}Sr_{0.2}MnO_3$)**	Hexagonal ($P6_3cm$)	57 %	a = b = 6.149(9) c = 11.390(15)	v = 373.093	2.71
	Cubic (Pm3m)	43 %	a = b = c = 3.814(5)	v = 55.502	
YSMO-50 **($Y_{0.5}Sr_{0.5}MnO_3$)**	Hexagonal ($P6_3cm$)	10 %	a = b = 6.149(8) c = 11.356(3)	v = 371.933	2.22
	Cubic (Pm3m)	90 %	a = b = c = 3.815(3)	v = 55.541	
YSMO-70 **($Y_{0.3}Sr_{0.7}MnO_3$)**	Hexagonal ($P6_3cm$)	4 %	a = b = 6.154(17) c = 11.366(6)	v = 372.796	2.49
	Cubic (Pm3m)	73 %	a = b = c = 3.812(5)	v = 55.393	
	Hexagonal ($P6_3/mmc$)	23 %	a = b = 5.451(7) c = 9.088(14)	v = 233.875	
YSMO-100 **($SrMnO_3$)**	Hexagonal ($P6_3/mmc$)	100 %	a = b = 5.451(4) c = 9.083(7)	v = 233.784	1.73

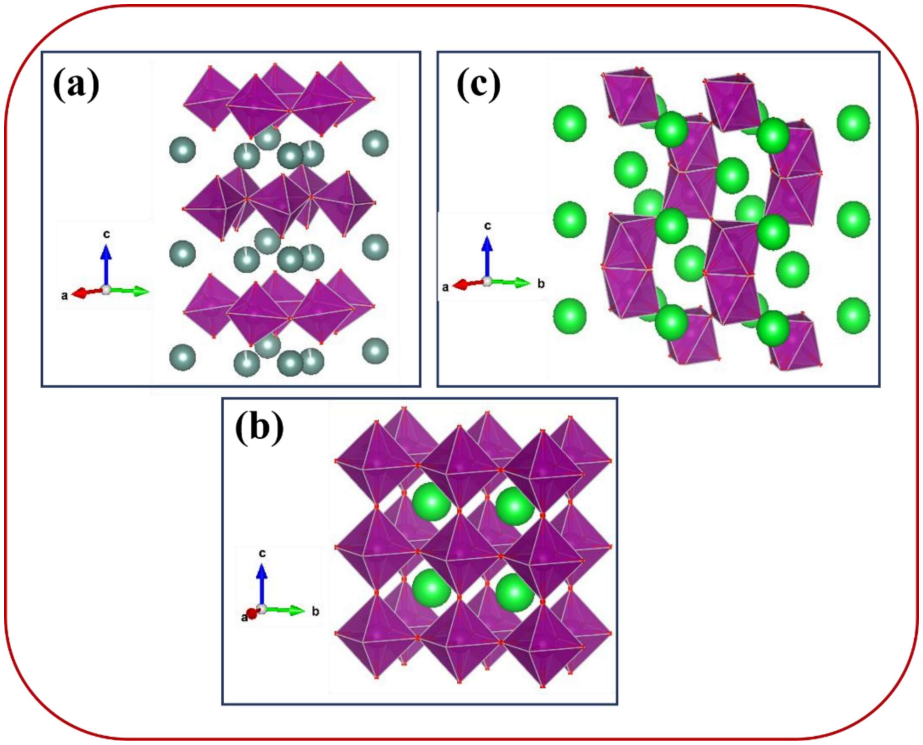

Figure 5.2: Crystal structure showing different pattern of MnO_6 octahedra in (a) YSMO-0, (b) YSMO-50, and (c) YSMO-100

The alternating short and long cationic radius at the A-site may lead to a serious mismatch of the MnO_6 octahedron, which results in the bending of the Mn-O-Mn bond angle and shortening of the Mn-O bond length [40]. In-turn, this yielded lattice distortion and Jahn-Teller effects in crystals along the c-axis. YSMO-50 was synthesized mostly in the cubic phase (90%) with small amount of hexagonal phase (10%).

5.3.2 XPS analysis

Fig. 5.3(a) represents the variation of Mn^{3+} and Mn^{4+} concentrations in different Sr-doped YSMOs samples, estimated through the core level spectra of Mn *2p*. As prepared materials show two chemical states of Mn, i.e. Mn^{3+} and Mn^{4+}. The 2*p*3/2 and 2*p*1/2 peaks at 642.4 eV and 654.0 eV respectively were ascribed to Mn^{3+}, and the 2*p*3/2 and 2*p*1/2 peaks observed at 644.0 eV and 655.5 eV were attributed to Mn^{4+}. Fig. 5.3(b) represents the core level XPS spectra of Sr 3*d*, Y 3*d*, Mn 2*p,* and O 1*s* of as prepared YSMO-50. It was found that the substitution of Y^{3+} by lower valance Sr^{2+} could regulate the oxygen vacancies and

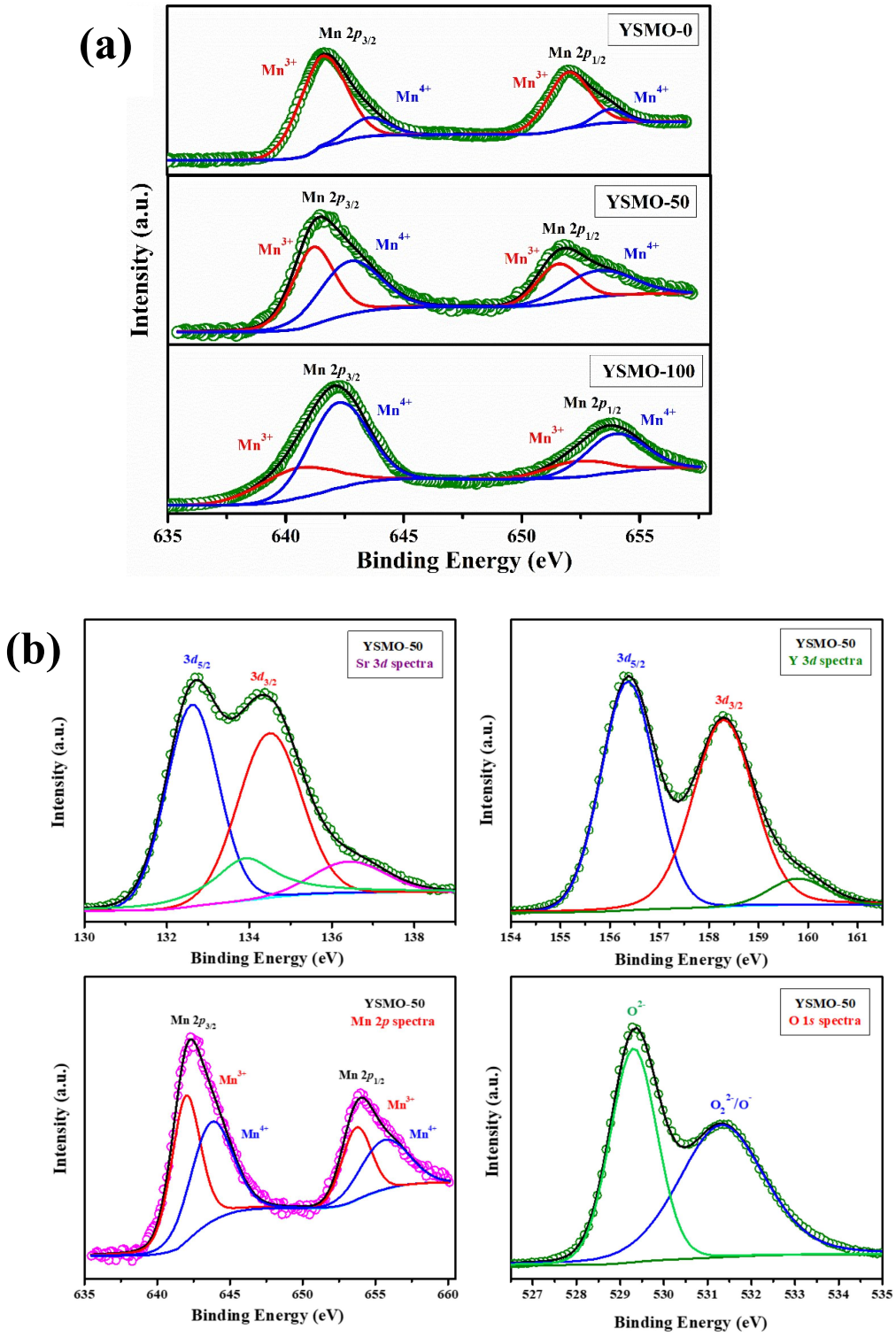

Figure 5.3: (a) the variation of Mn^{3+} and Mn^{4+} in core level XPS of different Sr-doped YSMO samples (YSMO-0, YSMO-50, and YSMO-100), (b) the core level XPS spectra of Sr 3d, Y 3d, Mn 2p, and O 1s of as-synthesized YSMO-50

Mn^{4+} concentration in $YMnO_3$ (as illustrated in Table 5.2) resulting in increased electrochemical performance in doped materials compared to pristine $YMnO_3$.

Table 5.2: Electronic structure of Mn in different composition of $Y_{1-x}Sr_xMnO_3$

	Mn^{3+} (%)	**Mn^{4+} (%)**
YSMO-0	88	12
YSMO-50	56	44
YSMO-100	82	18

5.3.3 Microstructural and morphological analysis

The morphology and particle size distribution of YSMO-50 was determined from scanning electron micrographs. The SEM image of YSMO-50, shown in Fig. 5.4(a) indicates that the particles are uniformly distributed in the entire region of the micrograph, and the selected area represents a different elemental colour mapping of Mn, O, Y, and Sr elements, as depicted in Fig. 5.4(b). The energy dispersive spectra, shown at the bottom of the SEM image, Fig. 5.4(c), confirms the presence of element Y, Sr, Mn, and O, and their corresponding atomic percentage are listed in Table 5.3, which confirms that the doping amount of Sr is substantially the same as the theoretical value in prepared materials. Further, the bright-field TEM image of YSMO-50 shown in Fig. 5.5(a) indicates inhomogeneous agglomerated nanoparticles, whose size roughly spans from 10 to 30 nm. The high resolution-TEM image, Fig. 5.5(b), displays lattice fringes with an inter-planar d-spacing of 0.27 nm corresponding to the (110) plane of cubic YSMO-50, which is in accordance with the theoretical value calculated by taking (110) diffraction peak of XRD data. The presence of distinct rings in the selected area electron diffraction (SAED) pattern, as shown in Fig. 5.5(c), indicates that the synthesized YSMO powders are poly-crystalline and the d-spacing calculated taking two collinear bright spots is 0.27 nm, which is in close agreement with the HR-TEM image.

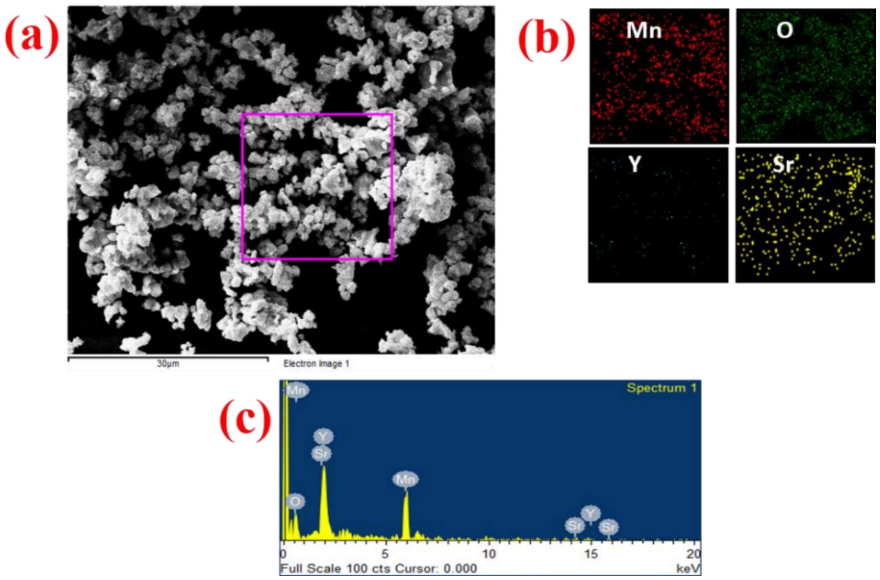

Figure 5.4: (a) SEM micrograph of as prepared YSMO-50, (b) and (c) elemental colour mapping and EDS spectrum of the selected area.

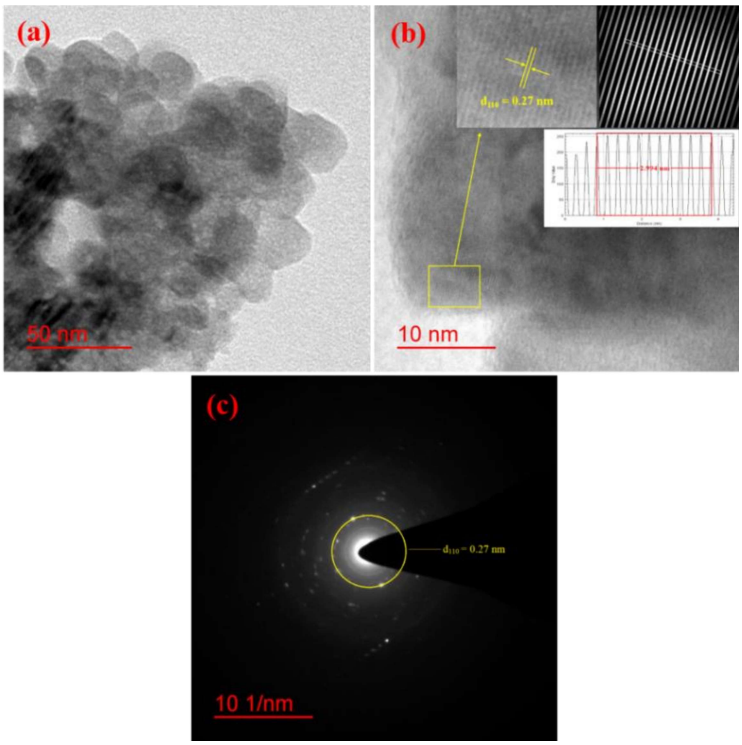

Figure 5.5: (a) bright-field TEM image, (b) HR-TEM with inter-planar d-spacing of (110) plane, (inset: inverse FFT of the selected region with their line profile), and (c) SAED pattern of YSMO-50.

Table 5.3: Compositional analysis of Ysmo-50 by the EDS

Composition	Y atomic %	Sr atomic %	Mn atomic %	O atomic %
YSMO-50	9.62	11.48	21.09	57.56

5.3.4 Surface area measurement

For pseudocapacitors, the materials with a high specific surface area are required to achieve higher capacitance through the redox reaction. Brunauer−Emmett−Teller (BET) surface area analysis has been carried out to get exact information about the surface area and porous nature of the materials. Fig. 5.6 represents the nitrogen adsorption/desorption isotherms and the corresponding pore size distribution curve (inset) for YSMO-50, which falls into the category of type IV and H_3 type hysteresis loop, which is a characteristic feature of a mesoporous material. The Barrett-Joyner-Halenda (BJH) model has been applied to get the average pore size of the material that lies in between the range of 2 to 10 nm. These might be linked to each other for the formation of agglomerated nanoparticles. The mesoporous nature of the material not only increases the surface area of the material but also shortens the ion diffusion path, therefore jointly facilitating the electrochemical reaction at the electrode surface. The specific surface areas of YSMO-0, YSMO-20, YSMO-50, YSMO-70 and YSMO-100 have been calculated to be 9.1, 16.3, 22.6 18.2 and 15.8 m^2g^{-1}, respectively. YSMO-50 shows the highest specific surface area among all the synthesized YSMOs.

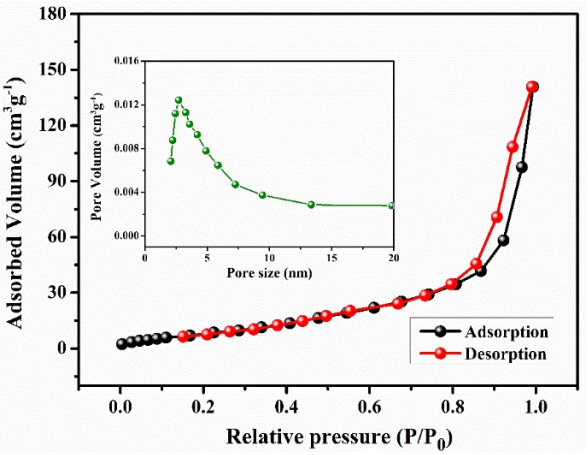

Figure 5.6: Nitrogen adsorption/desorption isotherm and corresponding pore size distribution curve (inset) of YSMO-50 powder.

5.3.5 Electrochemical measurements

The substitution of divalent cations (such as Sr^{2+}, Ca^{2+}) at the A site in $YMnO_3$ (ABO_3) perovskite systems may generate electron-hole at the B site. To maintain electrical neutrality, the valence state of manganese would change, releasing electrons outward and increasing the electrical conductivity of the material [203]. On the other hand, the electrochemical energy storage performance of the ABO_3 system is highly dependent on oxygen vacancy concentration, as proposed by Mefford et al. [117]. Thus, specific capacity could be increased by rising oxygen vacancies in ABO_3 perovskites. However, the electronic conductivity of perovskites could also be regulated by tuning the B-O-B bond angle and B-O bond length. When the angle tends to 180° and the length is shorter, an increased electrical conductivity is observed which can significantly improve the electrochemical energy storage performance of ABO_3 perovskites[204]. To verify the effect of Sr doping on the energy storage properties of $YMnO_3$, CV measurements were performed within the potential window of -0.8 V to 0.2 V vs Hg/HgO at 20 mV s^{-1} in a three-electrode cell, showed in Figure 5.7(a). The interaction between active material and substrate could affect electron transfer and surface redox reactions. A comparative study of nickel foam and carbon paper as current collectors indicated that the redox peaks of nickel foam were higher than those of carbon paper [205]. Therefore, carbon paper was selected as a substrate in the present work. At the same mass loading, the obtained large area of the CV curve implies a higher charge storage capacity of the material. The area under the CV curve of YSMO-50 was the largest, hence inducing the highest specific capacity among all samples. The specific capacity extracted from CV curves at 20 mV s^{-1} was found to be 33.04, 59.30, 87.07, 66.70, and 57.51 F g^{-1} for YSMO-0, YSMO-20, YSMO-50, YSMO-70, and YSMO-100, respectively.

Fig. 5.7(b) depicts the GCD curves of different YSMO samples scanned at a constant current density of 1 A g^{-1}. The GCD curves are asymmetric over the entire charge and discharge range and are composed of three regions with different slopes. The first continuous potential drop is due to the EDLC nature of the electrode, and the other two potential attenuations could be attributed to the redox process of the electrode. At the same current density, longer charge and discharge times would induce higher specific capacity. The specific capacity calculated from GCD curves at 1 A g^{-1} was 91.36, 189.73, 259.83, 213.86, and 177.67 F g^{-1} for YSMO-0, YSMO-20, YSMO-50, YSMO-70, and YSMO-100, respectively.

To gain a further understanding of the electrochemical performance, EIS tests were performed at open circuit potential to evaluate the kinetics and interface resistance of all the samples. The Nyquist plot combined with their equivalent circuit elements is shown in Fig. 5.7(c). The Nyquist plot represents the impedance characteristic as a function of frequency, which could be divided into two parts: a depressed semicircle corresponding to Faradaic reactions in the high-frequency region followed by a straight line in the low-frequency range. The intersection of the curve with the real axis at the high-frequency region represents the internal resistance (R_s), which includes the resistance of aqueous KOH electrolyte, active material, and connecting wires at the electrode-electrolyte interface. Whereas, in lower frequency region, a straight line with a slope different from 90° is related to the intercalation of ions within the modified electrode that maintains electrical neutrality during the surface redox reaction [206]. The R_s values of YSMO-0, YSMO20, YSMO-50, YSMO-70, and YSMO-100 electrodes were recorded as 2.01 Ω, 2.09 Ω, 1.45 Ω, 1.74 Ω, and 2.51 Ω, respectively. The lowest R_s of YSMO-50 indicated its highest diffusion ability. The diameter of the semicircle in the high/medium frequency region represents the charge transfer resistance for redox reaction and intrinsic conductivity of the modified electrode, as a very important factor that determines the power density of supercapacitors. The R_{ct} values of YSMO-0, YSMO-20, YSMO-50, YSMO-70, and YSMO-100 electrodes were estimated to be 12.47 Ω, 9.98 Ω, 6.94 Ω, 8.34 Ω and 11.5 Ω, respectively. The lowest R_{ct} value of YSMO-50 indicates its good electrochemical activity. In order to get the best fitting of EIS data, a constant phase element (CPE) was considered, and the results are summarized in Table 5.5. A higher value of Q_{lf} indicates a higher amount of intercalated electric charge within the electrode, hence exhibiting higher electroactive sites and low charge transfer resistance for redox reaction.

In summary, all the different strontium doped $YMnO_3$ samples exhibited much higher specific capacity compared to pristine $YMnO_3$. Hence, strontium-doping can increase the electrochemical performance of $YMnO_3$ as illustrated in Table 5.4. Samples doped with 50% strontium (YSMO-50) showed a superior energy storage performance of 259.83 F g^{-1}, which is 2.84-folds higher than $YMnO_3$ (91.36) at 1 A g^{-1} current density.

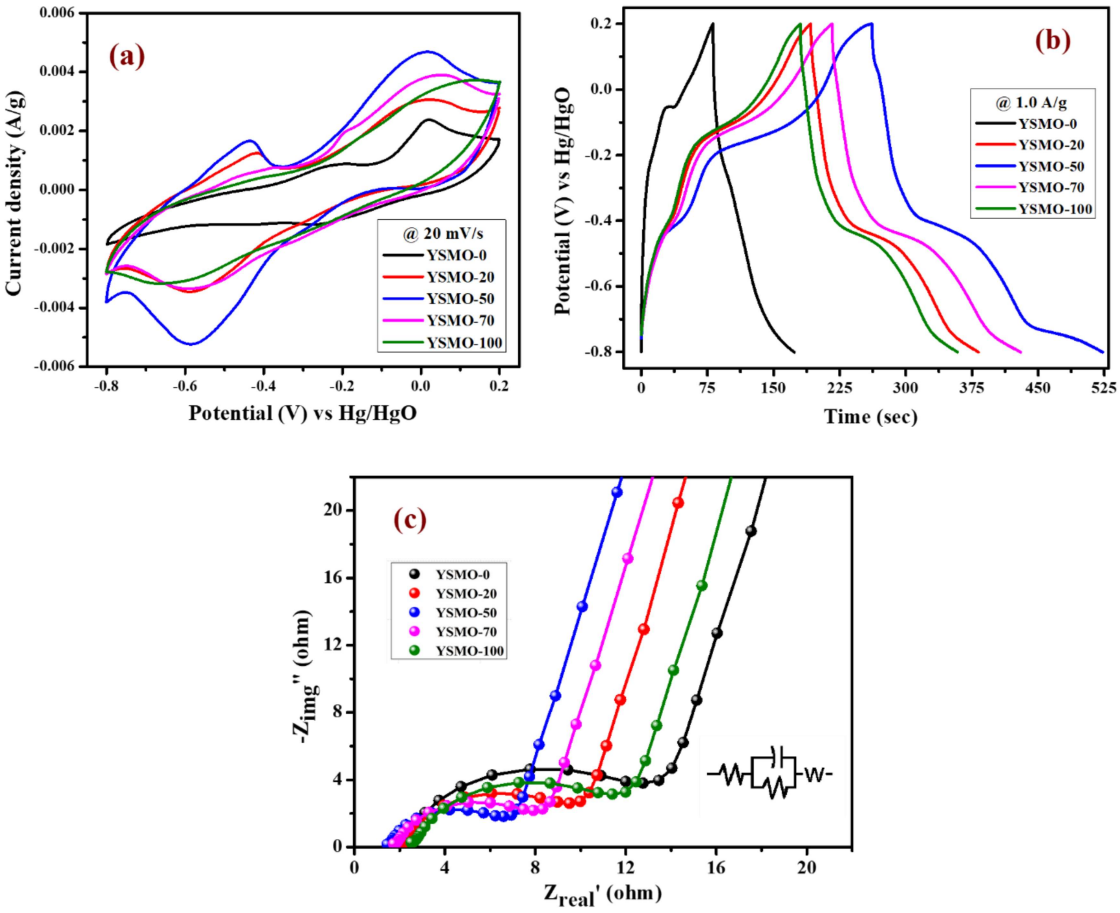

Figure 5.7: (a) CV at 20 mV s^{-1} scan rate, (b) GCD at 1 A g^{-1} current density, and (c) Nyquist plot at open circuit voltage of different electrodes viz. YSMO-0, YSMO-20, YSMO-50, YSMO-70, and YSMO-100.

Table 5.4: Specific charge storage capacitance of $Y_{1-x}Sr_xMnO_3$ electrodes

$Y_{1-x}Sr_xMnO_3$					
x	0.0	0.2	0.5	0.7	1.0
C_s(F/g) from CV @20 mV/s	33.04	59.30	87.07	66.70	57.51
C_s(F/g) from CD @1 A/g	91.36	189.73	259.83	213.86	177.67

5.3.6 Charge-discharge mechanism

The charge storage mechanism in perovskites could be completed through the cation reduction process, which leads to O^{2-} ions interconversion into OH^- through the incorporation or diffusion of water into the structure. The peaks at -0.25 and -0.6 V correspond to the reduction of Mn^{3+} to Mn^{2+}, and Mn^{4+} to Mn^{3+}, respectively. The peaks centered at -0.12 V and -0.42 V correspond to the oxidation of Mn^{2+} to Mn^{3+} and Mn^{3+} to Mn^{4+} respectively. The corresponding reversible redox reaction can be represented as:

$$Y_{0.5}Sr_{0.5}[Mn^{3+}_{0.5}; Mn^{4+}_{0.5}]O_{3-\delta} + 0.26\,[H_2O]_{ads} + 0.52\,e^- \leftrightarrow Y[Mn^{2+}_{0.09}; Mn^{3+}_{0.585}; Mn^{4+}_{0.325}]O_{2.867}[OH^-]_{0.52}$$

Table 5.5: Parameters of fitting of EIS of different composition of $Y_{1-x}Sr_xMnO_3$

$Y_{1-x}Sr_xMnO_3$				
x	**R_s (Ohm)**	**Q_{hf} (F n^{s-1}) (n = 0.74)**	**R_{ct} (Ohm)**	**Q_{lf} (F n^{s-1}) (n = 0.84)**
0.0	2.01	0.002663	12.47	0.01389
0.2	2.09	0.004736	9.98	0.02087
0.5	1.45	0.005836	6.94	0.03011
0.7	1.74	0.005232	8.34	0.02508
1.0	2.51	0.003596	11.5	0.01674

Fig. 5.8(a) represents CV curves of the YSMO-50 sample at various scan rates of 2, 5, 10, 20, and 50 mV s^{-1}. It may be noticed that the overall specific capacitance decreases as the scan rate increases. The oxidation and reduction peaks in CV curves were shifted continuously to higher and lower potentials with increasing scan rates, owing to the polarization effect of the electrodes. Further, we have examined the variation of specific capacitance of YSMO-50 as a function of constant current densities shown in Fig. 5.8(b). The charge-discharge curves are well consistent with CV results and the specific capacity obtained at different sweep rates and constant current densities are depicted in Table 5.6. The second oxidation peak appeared at -0.42 V is larger than the first, indicating that the main charge storage sites in YSMO-50 originated due to the oxidation of Mn^{3+} to Mn^{4+}, with massive adsorption of oxygen anions.

Table 5.6: Specific capacitance of YSMO-50 at various scan rates and current densities

YSMO-50						
Cyclic voltammetry	**Scan rate (mV/s)**	**2**	**5**	**10**	**20**	**50**
	Specific capacity (F/g)	241.12	152.79	121.84	87.07	43.72
Charge-discharge	**Current density (A/g)**	**0.5**	**1.0**	**2.0**	**3.0**	**5.0**
	Specific capacity (F/g)	407.18	259.83	189.43	114.70	79.14

Further, the amount of charge stored at the inner and outer surface of the YSMO-50 has been quantified separately, using the Power law [207]– [209] [48]– [50] and Trasatti plot. According to Power's law, the scan rate-dependent CV current can be expressed as:

$$i = a\upsilon^{b} \ldots\ldots (5.3)$$

$$\log i = \log a + b \log \upsilon \ldots\ldots (5.4)$$

where a and b are constants, their value depends upon the nature of the electrode material. In general b values lies between 0.5 to 1.0, which can be determined from the slope of the log(i) vs log(υ) plot. For a diffusion-controlled process, the b value is close to 0.5, while for a surface capacitive-controlled process, the b value approaches to 1.

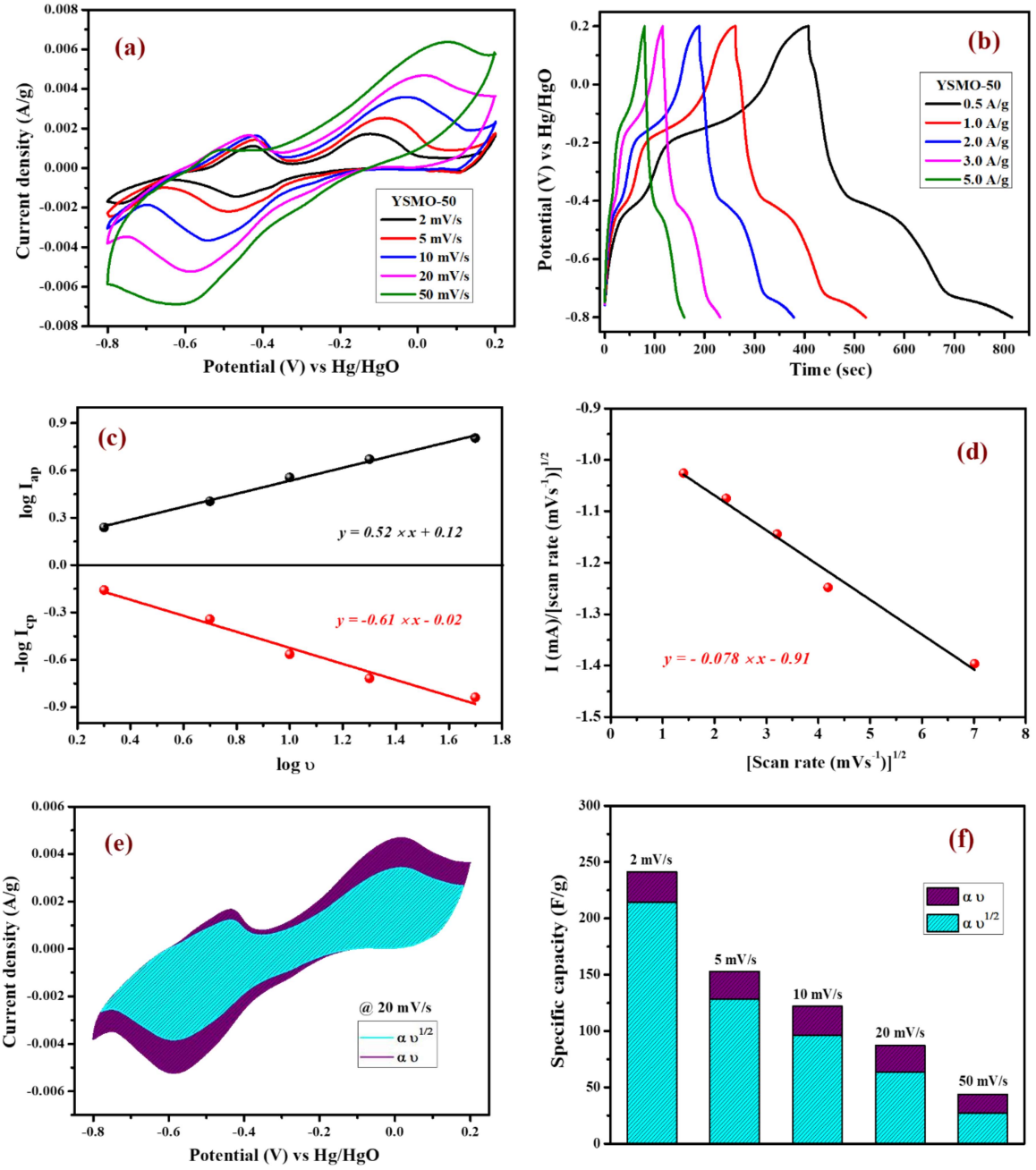

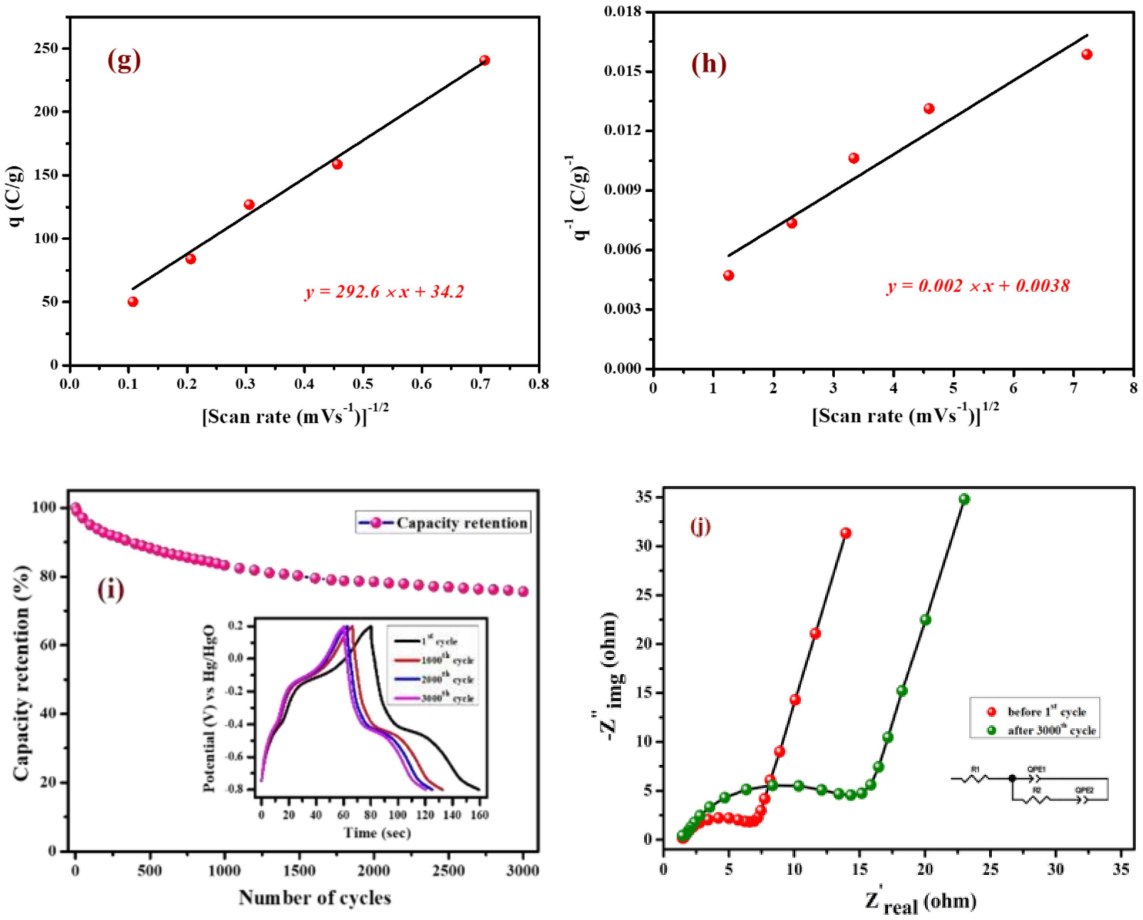

Figure 5.8: (a) CV at different scan rates starting from 2 mV s^{-1} to 50 mV s^{-1}, (b) GCD at different current densities from 0.5 A g^{-1} to 5 A g^{-1}, (c) plot between log i_{cp} and log i_{ap} vs log υ, (d) plot between $i/\upsilon^{1/2}$ vs $\upsilon^{1/2}$ at peak potential, (e) CV at 20 mV s^{-1} showing intercalation and surface contribution separately, (f) intercalation and surface contribution at different scan rate, (g) & (h) corresponds to the Trasatti plot of YSMO-50, (i) & (j) shows cyclic stability test of YSMO-50 and corresponding Nyquist plots taken before 1st and after 3000th cycle.

Fig 5.8(c) shows the log(*i*) vs log(*υ*) plot for the YSMO-50 electrode, and the obtained b value at anodic and cathodic peak potential is 0.52 and 0.61 respectively, which indicates the charge storage is mainly due to the diffusion-controlled process. Therefore, at a fixed potential, the charge storage contributions of the surface and diffusion process can be quantified separately by using the following relationship:

$$i(V) = k_1\upsilon + k_2\upsilon^{\frac{1}{2}} \ldots\ldots (5.5)$$

This can be further modified as-

$$\frac{i(V)}{\upsilon^{1/2}} = k_1\upsilon^{1/2} + k_2 \ldots\ldots (5.6)$$

where $k_1\upsilon$ and $k_2\upsilon^{1/2}$ correspond to the charge contributions from the surface effect and diffusion process, respectively. Thus, by determining the values of k_1 and k_2, from the slope and intercept of the plot between $\frac{i(V)}{\upsilon^{1/2}}$ and $\upsilon^{1/2}$, shown in Fig. 5.8(d), we can distinguish the percentage capacitive contribution of surface controlled-process (purple area) and diffusion controlled process (cyan area) of YSMO-50 sample, shown as a CV curve, Fig. 5.8(e). The percentage of capacitance that is contributed by the surface capacitive-controlled process of the YSMO-50 electrode is 11%, 16%, 21%, 27%, and 38% at scan rates of 2, 5, 10, 20, and 50 mV s^{-1}, respectively shown in bar diagram, Fig. 5.8(f).

Table 5.7: Parameters of fitting of EIS of YSMO-50 electrode (before and after cycling)

	YSMO-50			
	R_s (Ohm)	**Q_{hf} (F n^{s-1})**	**R_{ct} (Ohm)**	**Q_{lf} (F n^{s-1})**
Before cycling	1.45	0.005836(n = 0.74)	6.94	0.03011(n = 0.84)
After cycling	1.49	0.005048(n = 0.76)	14.31	0.01123(n = 0.88)

It is true that when the b value = 0.51, the capacity of the electrode material is mainly due to the diffusion-controlled process. However, the capacitance contribution percentage of the diffusion-controlled process gradually decreases with increasing scan rate because, at a higher scan rate, the inner part electrode has a negligible contribution to the redox reaction. This result indicates that the charge storage in YSMO-50 is mainly due to the conversion of Mn^{2+} to Mn^{3+} and Mn^{3+} to Mn^{4+}. We have further quantified the charge stored at the inner and outer surface of the electrode using the Trasatti plot. Figures 5.8(g) and 5.8(h) show the Trasatti plot of YSMO-50 electrodes. The y-intercept of the linear fit of q^{-1} vs $\upsilon^{1/2}$ at $\upsilon = 0$

represents the total amount of charge stored at the electrode (Fig. 5.8(h)), on the other hand, the y-intercept of the linear fit of q vs $\upsilon^{-1/2}$ at $\upsilon = 0$ shows the amount of charge stored at the outer surface of the electrode (Fig. 5.8(g)). So, the charge storage contribution for the inner structure of the electrode can be obtained as $Q_{total} - Q_{out}$. According to the Trasatti plot for YSMO-50, Q_{out} and Q_{in} are found to be 34 and 229 C g^{-1} respectively.

Furthermore, it is important to elucidate the cyclic performance of electrode material for its practical application as a supercapacitor electrode. The cyclic stability of YSMO-50 is tested up to the 3000^{th} cycle by applying continuous charge/ discharge current density at 5 A g^{-1} as illustrated in Fig. 5.8(i). The electrode exhibited 76% of capacity retention after the 3000^{th} cycle. The Nyquist plots, as given in Fig 5.8(j), show the better electrochemical performance of the fresh electrode compared to the cycled electrode, and the results extracted from the plots are summarized in Table 5.7.

Further, the post-mortem analysis has been carried out to see the effect of electrochemical cycling on the microstructure of YSMO-50. The sample was recovered by ultra-sonicating the coated electrode after the stability test. The SEM-EDS image of spent YSMO-50 given in Figure 5.9(a), does not show any appreciable changes in morphology and chemical composition, only the small particles that were not attached properly to the surface have been removed. Additionally, the HR-TEM image shown in Fig. 5.9(b) proves the long-term microstructure stability of synthesized YSMO-50. The inter-planar d-spacing corresponding to the (110) plane is found to be 0.27 nm, which is same as the freshly prepared YSMO-50. Above all the observations confirm that YSMO-50 can be an efficient, cheaper, and long-lasting electrode material for pseudocapacitor application.

To verify the change in the oxidation state of manganese during the electrochemical reaction, the XPS of YSMO-50 has been taken under the charged condition of 0.2 V and discharged condition of -0.8 V. The spectra of the tested sample did not contain any impurities except carbon and fluorine (they often came from activated carbon and PVDF).

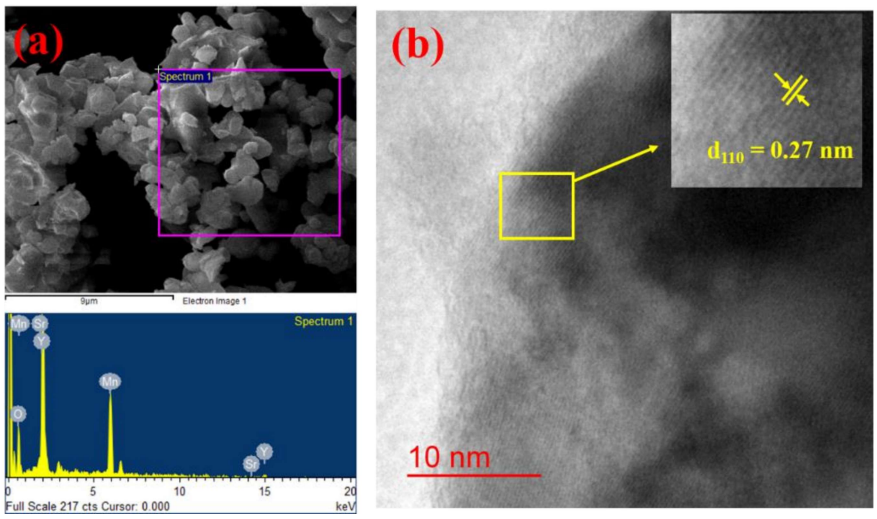

Figure 5.9: (a) represents SEM-EDS and (b) shows HR-TEM analysis of YSMO-50 after electrochemical cycling.

The deconvoluted Mn 2*p* spectra of discharged and charged electrodes exhibited three characteristic peaks at 641.8/653.1, 642.8/654.4, and 644.8/655.6 eV that corresponded to Mn^{2+}, Mn^{3+} and Mn^{4+} respectively as shown in Fig. 5.10(a) and their relative concentrations are listed in Table 5.8. From Table 5.8, it was observed that when the sample was discharged at -0.8 V, the relative concentration of Mn^{3+} increased and Mn^{4+} decreases with the slight formation of Mn^{2+}, which was further restored when the sample was charged at 0.2 V. At the end of each cycle relative concentration of Mn^{2+} keep on increasing with the expense of Mn^{4+} and the concentration of Mn^{3+} is almost consistent in perovskite, that resulted in partial irreversibility of YSMO-50 electrode.

Fig 5.10(b) represents the O1*s* spectrum of YSMO-50 charging at 0.2 V and discharging at -0.8 V and can be deconvoluted into four peaks: lattice oxygen species (O^{2-}) at 529.6 eV, highly oxidative oxygen species (O_2^{2-}/O^-) at 530.2 eV, hydroxyl groups (OH^-) at 531.6 eV and surface adsorbed H_2O at 532.4 eV. The relative concentration of O_{ads} species in the charged sample is much higher than that of the discharged sample, indicating that the partial cation of the Mn site deviates in the lattice during the charging, adsorbed hydroxide ions transfer its proton to a neighboring lattice oxide that may be oxidized into a peroxide-type species, O_2^{2-}, resulting higher concentration of O_{ads} was observed in charged YSMO-50.

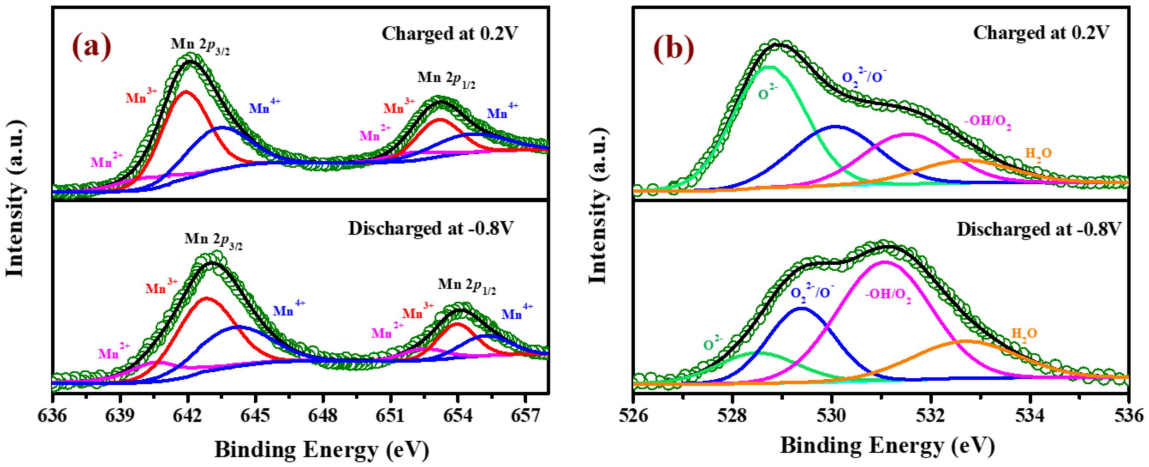

Figure 5.10: XPS pattern of YSMO-50 at a charging condition of 0.2 V and discharging condition of -0.8 V; (a) Mn 2p XPS spectra, (b) O 1s XPS spectra of the YSMO-50.

Table 5.8: Electronic structure of Mn of YSMO-50 from XPS study at different stage of charge and discharge

YSMO-50			
	Mn^{2+} (%)	**Mn^{3+} (%)**	**Mn^{4+} (%)**
Discharged at -0.8 V	2	60	38
Charged at 0.2 V	9	59	31

5.3.7 Full-cell asymmetric (YSMO-50//AC) testing:

To demonstrate the feasibility of YSMO-50 for its practical application in energy storage devices, an asymmetric cell (ASC) was fabricated using YSMO-50 as a negative and Activated carbon (AC) as positive electrodes and tested in PVA-KOH gel-electrolyte. From single electrode measurements, it is observed that YSMO-50 shows stable electrochemical performance within the potential range of 0.2 to -0.8 V, whereas activated carbon exhibits stable performance in the range of 0 to 0.8 V against the Hg/HgO reference electrode. To counterbalance the charge storage capacity of as fabricated ASC, the following Eq. has been used:

$$\frac{1}{C_{total}} = \frac{1}{C_{positive}} + \frac{1}{C_{negative}} \ldots\ldots (5.7)$$

$$\frac{m_+}{m_-} = \frac{C_-}{C_+}\frac{\Delta V_-}{\Delta V_+} \ldots\ldots (5.8)$$

where m_+, C_+, ΔV_+ m_-, C_-, and ΔV_- are the mass, specific capacitance, and potential window of the positive and negative electrodes, respectively, estimated by the single electrode experiment [52][53]. The calculated mass ratio (m_+ /m_-) was found to be 2.13:1 for the asymmetric cell. Figure 5.11(a) shows the individual CV of AC (black curve) and YSMO-50 (red curve) at a 20 mV s^{-1} scan rate. Figure 5.11(b) demonstrates the CV curve YSMO-50 //AC (ASC) at different scan rates, ranging from 2 to 50 mV s^{-1} in the stable potential window of 0 to 1.8 V, which exhibits a redox reaction of Mn^{3+} to Mn^{4+}. Figure 5.11(c) shows the charge/discharge curve for the YSMO-50//AC electrode at different constant current densities of 0.5, 1, 2, 3 and 5 A g^{-1}. The capacitance value calculated using the CV and GCD curve is listed in Table 5.9. Figure 5.11(d) shows the stability test of the YSMO-50 electrode in a full-cell mode that exhibited 68.2% capacity retention after 3000th times charge/discharge at a current density of 5 A g^{-1}. Figure 5.11(e) shows the Nyquist plot in the frequency range 100 kHz to 0.1 Hz at open circuit voltage, confirming the superior charge transfer and higher specific capacitance of YSMO-50//AC in full-cell mode. However, a minor capacity fading is observed during the cyclic test because of the partially irreversible nature of the electrode. The specific energy and specific power of the asymmetric capacitor are calculated using the following equations:

$$E\ (Wh\ kg^{-1}) = \frac{0.5\ \times C_{ASC} \times \Delta V^2}{3.6} \ldots\ldots (5.9)$$

$$P\ (W\ kg^{-1}) = \frac{E \times 3600}{t_{dis}} \ldots\ldots . (5.10)$$

where C_{ASC} is the specific capacitance, V is the operating voltage window, and t_{dis} is the discharge time. Fig. 5.11(f), shows the plot of specific energy vs specific power at different constant current densities. The result showed that at 0.5 A g^{-1} current density YSMO-50//AC exhibited 65.13 Wh kg^{-1} specific energy and 0.45 kW kg^{-1} specific power, whereas when the current density was raised to 5 A g^{-1}, the ASC exhibits specific power of 4.5 kW kg^{-1} with specific energy ~7.76 Wh kg^{-1}.

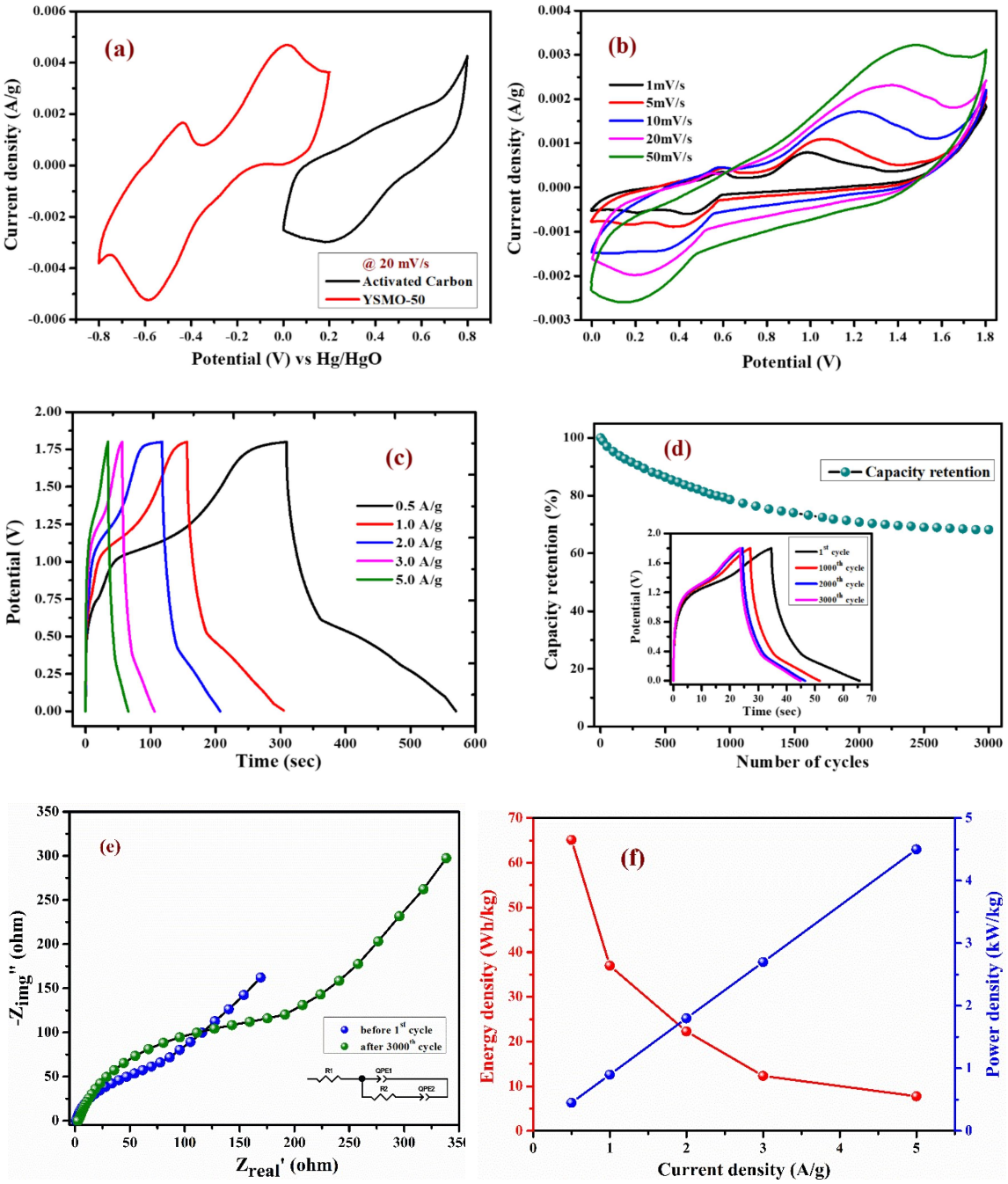

Figure 5.11: (a) individual CV curves of YSMO-50 and AC electrodes in a three electrode cell set up at 20 mV s^{-1} scan rate, (b) CV curves of YSMO-50//AC recorded as a function of scan rates, (c) Charge/discharge profile at different current densities, (d) Cyclic test of ASC cell at 5 A g^{-1} current density up to 3000th cycles, (e) Nyquist plots of ASC cell recorded before 1st and after 3000th cycles, and (f) Ragone plot of ASC device

Table 5.9: Specific capacitance of ASC type YSMO-50//AC full cell at various scan rates and current densities

YSMO-50//AC						
Cyclic voltammetry	**Scan rate (mV/s)**	**2**	**5**	**10**	**20**	**50**
	Specific capacity (F/g)	107.22	64.78	56.05	39.25	20.92
Charge-discharge	**Current density (F/g)**	**0.5**	**1.0**	**2.0**	**3.0**	**5.0**
	Specific capacity (F/g)	144.74	82.20	49.45	27.36	17.25

Table 5.10 summarizes the different values of capacitances and resistances of fresh and cycled electrodes extracted from the Nyquist plots.

Table 5.10: Parameters of fitting of EIS of ASC type YSMO-50//AC full cell electrodes (before and after cycling)

YSMO-50 // AC				
	R_s (Ohm)	**Q_{hf} (F n^{s-1})**	**R_{ct} (Ohm)**	**Q_{lf} (F n^{s-1})**
Before cycling	1.103	0.001326(n = 0.85)	107	0.06801(n = 0.63)
After cycling	2.739	0.0005563(n = 0.83)	256	0.004201(n = 0.70)

5.4 Conclusion

$Y_{1-x}Sr_xMnO_{3-\delta}$ (x = 0, 0.2, 0.5, 0.7, and 1.0) were prepared by the solid-state ceramic route and investigated as a pseudocapacitor electrode for supercapacitors. $Y_{1-x}Sr_xMnO_3$ with x = 0.50 (YSMO-50) exhibited the highest specific capacitance of 259.83 F g^{-1} at 1 A g^{-1} current density and lower intrinsic resistance of 1.45 Ω cm^{-2}. The pseudocapacitance in the YSMO-50 electrode is attributed mainly due to the surface redox reaction of Mn^{2+}/Mn^{3+} and Mn^{3+}/Mn^{4+} during the charge-discharge process. The reason behind the enhanced capacity of YSMO-50 is the doping of low valence strontium atom in $YMnO_3$, which results in the transformation of crystal structure from hexagonal to cubic and facilitates the formation of oxygen vacancy in $YMnO_3$. During the cyclic test, a serious cation leaching problem occurs that causes slight fading of specific capacity. The presented results indicate that YSMO-50 material exhibited superior capacitive performance (259.83 F g^{-1}) through the interconversion of O^{2-} to OH^- mechanism. Further, in an asymmetric mode, YSMO-50//AC exhibited a maximum energy density of 65.13 Wh kg^{-1} and power density of 0.45 kW kg^{-1} at a specific capacity of 144.74 F g^{-1}. Here, the presented results demonstrate that Sr-doped $YMnO_3$ perovskites may be a potential candidate to be used as electrode material in fast energy storage technology.